Performance of Recent Large-angle Extensions to Classical Simulator Washout Algorithms

M. Micomonaco
M.A.Sc.

R.A. Irani
Professor

M.J.D. Hayes
Professor

R.G. Langlois
Professor

Carleton University
Department of Mechanical and Aerospace Engineering
Ottawa, ON, Canada

ABSTRACT

Washout algorithms are typically used in flight simulator motion control software to give the pilots flying the simulator the impression that they are experiencing an unlimited range of motion when the Gough-Stewart hexapod providing the motion cues has a comparably very small motion envelope. Since hexapods have generally been adopted by the motion simulator industry and the washout algorithms developed in the 1970s have performed extremely well at giving pilots a very high fidelity training experience despite the very small angular workspace of the motion platforms, research in the area generally came to a halt in the 1980s. We have succeeded in development of the Atlas motion platform which possesses an unbounded orientation workspace that is singularity free, hence we have the need to revisit washout algorithm development to take advantage of the unlimited orientation workspace. In this paper, after a brief review of existing approaches, we outline the development of our unlimited angular washout. Several benchmark cases are presented for two aircraft having very different flight characteristics: a Cessna 172 and a Columbia 400. Additionally, a quantitative comparison of small, large, and unlimited angular washout algorithm performance is reported.

INTRODUCTION

Typical flight simulators are limited by their motion envelope and to mimic a wider range of motion, "washout algorithms" are commonly used. A washout algorithm attempts to recreate the pilot or passenger's perception of the angular velocity and specific force that they would experience during flight. The algorithm takes advantage of the human perception for motion; thus, the angular velocity components of the aircraft simulation focuses on the high-frequency motion cues while the specific force components are achieved by a combination of translational acceleration and rotation. The translational accelerations are limited to short and sudden movements to simulate the high-frequency specific force cues associated with a motion's onset. In conjunction, a coordinated tilt is used to simulate the sustained specific forces by slowly rotating the simulator, below the human perception, such that the pilot experiences a sustained force from the gravity vector. The outcome of the washout algorithm is the combined translational and rotational motions that allow for the simulation of motion onset and sustained specific force that would not be possible otherwise.

The classical washout algorithm of Reid and Nahon (Refs. 1–3) uses high-pass filters for the determination of the high-frequency specific force and angular velocity cues, while low-pass filters define the cues for the sustained translational acceleration. Since classical washout is intuitive and easy to

tune, the algorithm is commonly used in the flight simulator industry. A Gough-Stewart platform is the defacto motion base for flight simulators and these platforms have restricted angular displacement in all directions. Thus, washout algorithms have been developed with these angular restrictions in mind and utilise several small-angle approximations and are limited in their angular outputs.

There is an increasing desire for training at the edge-of-envelope aircraft motions (Ref. 4) and so simulators with larger or limitless angular motion envelopes are being developed. Moreover, limitless angular motion envelopes are of interest to helicopter simulations as the unrestricted rotational envelope allows for repeated and sustained yaw manoeuvres. An example of a limitless rotational system is the Atlas motion simulator developed by the Carleton University Simulator Project (CUSP), which has unbounded rotation on all axes (Refs. 5–7). To take advantage of the unbounded rotation, several modifications are required to the classical washout algorithm.

The work herein extends and assesses classical washout to large angles and the performance is evaluated. Starting with classical washout, all small-angle approximations are removed and the full nonlinear equations are utilized. Due to the geometry of a freely rotating simulator, such as Atlas, the tilt coordination can now act on all degrees of freedom, allowing for the motion base to respond appropriately for all orientations. Quaternions replace traditional Euler angles for the simulator's kinematics, which eliminates the representational singularities present in Euler formulations (Ref. 8). Finally,

1

the high-pass filters of the algorithm are removed from the rotational channel so that the system is unrestricted to angular velocity cues.

The current paper is divided into eight sections. The following section presents a brief background of the use of classical washout algorithms and the vestibular system that are used to simulate a human pilot. A detailed explanation of classical washout is presented in the follow-on section. As an extension to classical washout, the paper proposes two theoretical extensions of the washout algorithm known as "large-angle washout" and "unrestricted washout". The extensions are examined and compared through a set of metrics which are used in series of case studies. The paper concludes with a discussion of the results.

BACKGROUND - WASHOUT ALGORITHMS

Limited advancements to the washout algorithms have been made since the extensive Reid and Nahon studies (Refs. 1–3). Many researchers have focused on the evaluation and tuning of the washout algorithm (Refs. 9–13). In the comprehensive Reid and Nahon studies, they developed multiple benchmark cases for each algorithm type: classical washout, adaptive washout, and optimal control, then subjected the algorithms to extensive testing. Adaptive and classical washout both performed well, with adaptive washout subjectivity ranked best by the pilots. Meanwhile, optimal control produced poor results in the testing (Refs. 1–3). Thus, within the current work, classical washout will be expanded to accommodate large angles, due to its extensive use (Ref. 13), acceptable performance and limited parameter space when compared to adaptive washout (Refs. 1–3).

Classical washout can be implemented with two different versions, using high-order or low-order filters. The high-order filters act to recentre the motion simulator during sustained translational accelerations, allowing for the full motion envelope to be available in all directions. The low-order filters do not recentre the simulator, which reduces the available motion envelope but also reduces the negative motion cues experienced by the pilot due to the simulator motion. As the current work is focusing on extending the rotational envelope, the low-order filters version of classical washout will be used. The proposed rotational extension can assist in rotorcraft pilot training and assess the impact of sustained motion cues on them.

In recent years, Keshavarz et al. (Ref. 14), using the classical washout algorithm, evaluated the impact motion, visual, and auditory cues have when experiencing motion sickness in driving simulators. Cleij et al. (Ref. 15) used classical washout to examine how individuals respond to negative cues within simulators. Studying pilot response but with rotorcraft and an unaltered classical washout, Dalmeijer et al. (Ref. 16) explored testing methods for evaluating a flight simulator's performance. The goal of these simulators is achieving motion cues so that the pilot perceives the same experience as they would in an aircraft; thus, in simulation and development of flight simulator and washout algorithms, a vestibular model is critical as it emulates the pilot's perception (Ref. 3). The vestibular system consists of two parts: 1) the otolith that detects translational specific force, and 2) the three semicircular canals, lateral, anterior and posterior, that detect rotational motion.

Examining the otolith system, Meiry and Young (Ref. 17) developed a pair of transfer functions with a deadband between them to represent the threshold where the specific force can be detected. Zacharaias (Ref. 18) conducted a review of vestibular models and proposed reasonable threshold values for specific force detection. The first report of Reid and Nahon (Ref. 1) utilized the Meiry and Young model but with the deadband values from Zacharias to model the pilot's specific force perception. However, in the second phase of Reid and Nahon's study (Ref. 2) the deadband when graphing the vestibular response of the simulator and aircraft pilots was no longer included. In 2016, Asadi et al. (Ref. 19) completed a survey of otolith models and includes the Meiry and Young model used by Reid and Nahon. Asadi et al. (Ref. 19) recommend the Telban and Cardullo model, which when compared to Meiry and Young with the deadband values of Zacharaias (Ref. 18), reduces the gain and phase lag for perceiving lower-frequency specific force. However, to maintain consistency between the results of the current work and the original Reid and Nahon reports (Refs. 1–3), the Meiry and Young model will be used.

To model the semi-circular canals response to angular acceleration motions, Young and Oman (Ref. 20) developed a transfer function model. As before, Zacharaias (Ref. 18) proposed the detection threshold deadbands which can be used in conjunction with the Young and Oman model for angular velocity. Again, in the early work of Reid and Nahon, they use the Young and Oman model with the deadbands; however, in their second phase, they omit the deadbands in the vestibular response presentation. In 2017, Asadi et al. (Ref. 21) complimented their previous study and conducted a survey of semicircular canal vestibular models. They concluded that the Young and Oman model, used by Reid and Nahon, as well as the Telban and Cardullo model, were both reasonable models for the semicircular canal experiencing normal head movement. However, the Telban and Cardullo model was stated to be the more acceptable. As with the otolith system model selection, to maintain consistency the current work will use the Young and Oman model so that a direct comparison with Reid and Nahon's classical washout is possible.

TRADITIONAL CLASSICAL WASHOUT FORMULATION

Figure 1 illustrates the block diagram of classical washout, where the translational, tilt coordination, and rotational channels are indicated. From an aircraft model, the washout algorithm takes in inputs of the specific force and angular velocity experienced by the aircraft pilot, and produces set points of the translational and angular positions for the motion simulator.
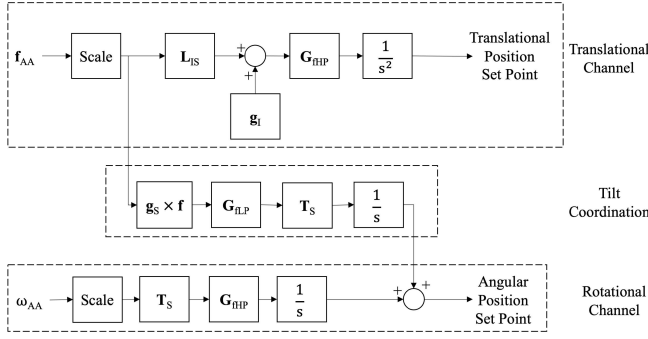
Figure 1. Classical washout with Euler angles

Translational Channel

The input of the translational channel, the specific force experienced by the simulators pilot, is in the aircraft frame. First, the specific force may be optionally scaled, to assist in ensuring that the simulator motion set point remains within the hardware limits of the motion simulator. It is then converted into the inertial frame using the rotation matrix L_{IS}

$$L_{IS} = \begin{bmatrix} c(\theta)c(\psi) & \begin{matrix} s(\phi)s(\theta)c(\psi)- \\ c(\phi)c(\psi) \end{matrix} & \begin{matrix} c(\phi)s(\theta)c(\psi)+ \\ s(\phi)s(\psi) \end{matrix} \\ c(\theta)s(\psi) & \begin{matrix} s(\phi)s(\theta)c(\psi)+ \\ c(\phi)c(\psi) \end{matrix} & \begin{matrix} c(\phi)s(\theta)c(\psi)- \\ s(\phi)s(\psi) \end{matrix} \\ -s(\theta) & s(\phi)c(\theta) & c(\phi)c(\theta) \end{bmatrix} \quad (1)$$

where ϕ, θ, and ψ are the roll, pitch, and yaw Euler angles consistent with the *ZYX* rotation sequence based on the current orientation of the simulator (Ref. [1]). Gravity g_I is added in the inertial frame to convert the specific force to acceleration, and the result is then passed through a high-pass filter G_{fHP} of the form

$$G_{fHP} = \frac{s^2}{(s+\omega_n)^2}. \quad (2)$$

The output of the high-pass filter is then integrated twice to produce a translational position set point while the output of the optional scaling is the input to the tilt coordination.

Tilt Coordination

While the translational channel simulates the high-frequency specific forces, tilt coordination acts to simulate the low-frequency sustained specific forces. To simulate sustained specific forces, tilt coordination aligns the gravity vector with the direction of the specific force. Reid and Nahon discuss two methods of tilt coordination (Ref. [1]). One method, as illustrated in Figure [1], involves taking the cross product of g_S, the gravity vector in the simulator frame, and the scaled specific force f_{AA}. The result is then multiplied by a scaling factor such that the result is an angular velocity which will align the gravity vector with the specific force set point without overshoot. As the simulator's rotation rate must be below the threshold that the pilot will detect, it is passed through a low-pass filter of the form

$$G_{fHP} = \frac{4\omega_n^2}{s^2 + 4\omega_n s + 4\omega_n^2}. \quad (3)$$

A rate limiter can also be added after the integrator if required to ensure the rotation produced by tilt coordination is below the pilot's perception threshold. The filtered angular velocity is converted to Euler angular rates using

$$T_s = \begin{bmatrix} 1 & s(\phi)t(\theta) & c(\phi)t(\theta) \\ 0 & c(\phi) & -s(\phi) \\ 0 & s(\phi)\sec(\theta) & c(\phi)\sec(\theta) \end{bmatrix} \quad (4)$$

based on the current orientation of the simulator, and then integrated to update the Euler angles (Ref. [1]).

An alternative tilt coordination method, which is not used in the current work, relies on small-angle simplifications (Ref. [1]). The small-angle tilt coordination channel illustrated in Figure [1] can instead be modelled by removing $g_s \times f$, T_s, and the integrator and in their place inserting

$$\begin{bmatrix} \phi & \theta & \psi \end{bmatrix}^T = \begin{bmatrix} \frac{-f_y}{g} & \frac{f_x}{g} & 0 \end{bmatrix}^T \quad (5)$$

after G_{fLP}. Thus, the small-angle tilt coordination is reduced to a low-pass filtering of the scaled f_{AA} feeding the small-angle approximation from Equation [5].

To keep the motions at an acceptable level, a rate limiter can be placed after the integrator of T_s or Equation [5]. The output of the tilt coordination is used within the rotational channel.

Rotational Channel

To simulate the angular velocity experienced by the aircraft pilot, the rotational channel takes the input of angular velocity in the aircraft frame. It is scaled, if required, and converted to Euler angular rates using Equation [4]. The Euler angular rates are passed through a high-pass filter of the form

$$G_{fHP} = \frac{s}{(s+\omega_n)} \quad (6)$$

where ω_n is chosen based on the desired performance characteristics.

The output of G_{fHP} is integrated to produce angular position, and is then added to the Euler angles produced from the tilt coordination. The addition of Euler angles from the tilt coordination and rotational channels is not strictly mathematically correct, but is an acceptable approximation for small angles (Ref. [1]). The sum of the Euler angles is the angular position set point.

3
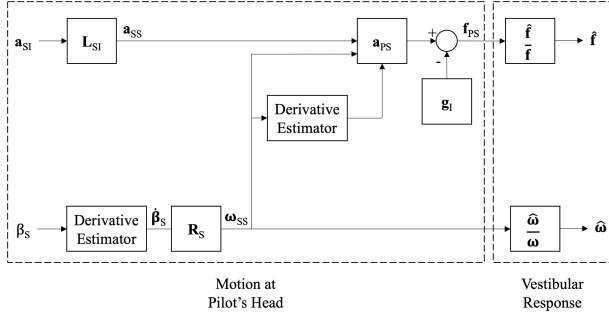
Figure 2. Vestibular response block diagram.

Washout Parameters

To populate the various filters, Reid and Nahon developed three classical washout parameter sets, with different simulator response characteristics (Ref. 2). However, for the contents of this work only the first CW1 (Ref. 2) is particularly germane and Table 1 lists the parameters for the filters which were used. For the CW1 set in the surge degree of freedom,

Table 1. Classical washout parameter sets.

Parameter Set	DOF	ω_n [deg/s]
	Surge	1.5
CW1	Sway, Heave	3.5
	Roll, Pitch, Yaw	0.5

the parameters result in the translational channel high-pass filter and tilt coordination low-pass filter having a cutoff frequency of 0.31 Hz for the low-pass filter and 0.37 Hz for the high pass filter.

Vestibular Response

The pilot's vestibular system allows the pilot to perceive changes in specific force and angular velocity. To accurately simulate aircraft motion, the simulator needs to reproduce similar vestibular responses in the simulator pilot as would have been experienced by the aircraft pilot. Figure 2 illustrates the block diagram to determine the motion at the pilot's head and the pilot's vestibular response to motion. The simulator's translational acceleration in the inertial frame a_{SI} and angular position expressed in Euler angles β_S are the inputs. The specific force at the pilot's head f_{PS} and the angular velocity of the simulator ω_{SS} are calculated, and input into the vestibular response model, which calculates the vestibular response to the specific force and angular velocity.

Simulator Motion

The inputs to the vestibular system are the specific force and angular velocity experienced by the simulator pilot's head. For a physical simulator, the translational acceleration in the

inertial frame a_{SI} and the angular position expressed using Euler angles $\beta_S = [\phi,\ \theta,\ \psi]^T$ are measured. For the developmental numerical simulations, it is assumed that the simulator has perfect response to a given set point.

To calculate the specific force applied to the simulator pilot, f_S, the acceleration is first converted into the simulator frame using the rotation matrix

$$L_{SI} = \begin{bmatrix} c(\theta)c(\psi) & c(\theta)s(\psi) & -s(\theta) \\ \begin{matrix} s(\phi)s(\theta)c(\psi)- \\ c(\phi)c(\psi) \end{matrix} & \begin{matrix} s(\phi)s(\theta)s(\psi)+ \\ c(\phi)c(\psi) \end{matrix} & s(\phi)c(\theta) \\ \begin{matrix} c(\phi)s(\theta)c(\psi)+ \\ s(\phi)s(\psi) \end{matrix} & \begin{matrix} c(\phi)s(\theta)s(\psi)- \\ s(\phi)c(\psi) \end{matrix} & c(\phi)c(\theta) \end{bmatrix} \quad (7)$$

which is the inverse of Equation 1, to give the simulator acceleration in the simulator frame a_{SS}.

The equation

$$G_{est} = \frac{s\omega_2}{s + \omega_2} \quad (8)$$

where $\omega_2 = 12.5$ rad/s is used to estimate a derivative and used to estimate the rate of change for the Euler angles. The rate of change of Euler angles of the simulator is then converted into angular velocities, $\omega_{SS} = [p_{SS},\ q_{SS},\ r_{SS}]^T$, using the matrix

$$R_S = \begin{bmatrix} 1 & 0 & -s(\theta) \\ 0 & c(\phi) & s(\phi)c(\theta) \\ 0 & -s(\phi) & c(\phi)c(\theta). \end{bmatrix} \quad (9)$$

The angular acceleration, $\dot{\omega}_{SS} = [\dot{p}_{SS},\ \dot{q}_{SS},\ \dot{r}_{SS}]^T$, is estimated with the derivative estimaton, Equation 8. The acceleration at the aircraft pilot's head is calculated using

$$a_{PS} = a_{SS} + \begin{bmatrix} -(q_{SS}^2 + r_{SS}^2) & p_{SS}q_{SS} - \dot{r}_{SS} & p_{SS}r_{SS} + \dot{q}_{SS} \\ p_{SS}q_{SS} + \dot{r}_{SS} & -(p_{SS}^2 + r_{SS}^2) & q_{SS}r_{SS} - \dot{p}_{SS} \\ p_{SS}r_{SS} - \dot{q}_{SS} & q_{SS}r_{SS} - \dot{p}_{SS} & -(p_{SS}^2 + q_{SS}^2) \end{bmatrix} R_{SS}$$

where the vector R_{SS} is the displacement of the pilot's head from the origin of the simulator reference frame (Ref. 1). For the Atlas simulator $R_{SS} = [0,\ 0,\ 0]^T$ as the pilot's head is positioned at the geometric centre of the simulator cockpit. With the resulting acceleration, the specific force at the pilot's head, f_{PS} is calculated using

$$f_{AA} = a_{AA} - g_{AA} \quad (10)$$

where g_{AA} is the gravity vector in the aircraft frame, and the positive z axis is pointing downward. For clarity, Table 2 lists some examples of the relationship between a_{AA} and f_{AA}.

Table 2. Relationship between a_{AA} and f_{AA}.

	Rest	1g Down (Freefall)	1g Up
a_{AA}	$[0,0,0]^T$	$[0,0,g]^T$	$[0,0,-g]^T$
g_{AA}	$[0,0,g]^T$	$[0,0,g]^T$	$[0,0,g]^T$
f_{AA}	$[0,0,-g]^T$	$[0,0,0]^T$	$[0,0,-2g]^T$

Within the numerical simulation, the output of the simulator motion which utilizes the washout algorithm becomes the input to the vestibular system which approximates the pilot's response.

Vestibular System

The primary organs in the human body for sensing specific force and rotational motion are the otolith and the semicircular canals, respectively. The otolith response to specific force $\hat{f}$ can be modelled as the transfer function

$$\frac{\hat{f}_i}{f_i} = \frac{K\tau_a s + 1}{(\tau_L s + 1)(\tau_s s + 1)} \qquad (11)$$

with typical parameter values of $\tau_L = 5.33$ s, $\tau_S = 0.66$ s, $\tau_a = 13.2$ s, and $K = 0.4$ (Ref. 1).

The semicircular canal response to angular velocity can be modelled as the transfer function

$$\frac{\hat{\omega}_i}{\omega_i} = \frac{T_L T_a s^2}{(T_L s + 1)(T_S s + 1)(T_a s + 1)} \qquad (12)$$

with typical parameter values of $T_L = 10.2$ s, $T_S = 0.1$ s, and $T_a = 30.0$ s (Ref. 1).

Now with traditional classical washout defined, we propose an extension to account for a large-angle and a new unrestricted angular motion washout formulation.

LARGE-ANGLE WASHOUT

Classic washout algorithms are designed for small angular motions; therefore, problems arise as the range of angular displacement increases. There are several limitations that the small-angle classical washout experiences when used for large angular motions. Euler angles, regardless of the sequence used, will always have a singularity when the middle angle of the sequence reaches $\frac{\pi}{2} \pm i\pi$ where i is any positive integer. Furthermore, the addition of the Euler angles from the tilt coordination and rotational channels to produce the angular position set point, which was an acceptable approximation at small angles (Ref. 1), will cause significant error with larger angular displacements.

Large-angle washout uses a similar form to the small-angle classical washout block diagram, which was illustrated in Figure 1. The Euler angles are replaced with unit quaternions, which are a form of specifying 3D rigid body orientation that is free of representational singularities, where

$$\boldsymbol{q} = \begin{bmatrix} q_0 \\ \boldsymbol{q_v} \end{bmatrix} = \begin{bmatrix} q_0 \\ q_1 \\ q_2 \\ q_3 \end{bmatrix} = \begin{bmatrix} \cos(\theta/2) \\ k_x \sin(\theta/2) \\ k_y \sin(\theta/2) \\ k_z \sin(\theta/2). \end{bmatrix} \qquad (13)$$

and the change in orientation relative to three mutually orthogonal basis vectors can be viewed as a single rotation through angle θ about the equivalent axis $\boldsymbol{k} = [k_x, k_y, k_z]$. The unit quaternion must also satisfy the condition

$$q_0^2 + q_1^2 + q_2^2 + q_3^2 = 1. \qquad (14)$$

Use of a quaternion for orientation is considered to be free from representational singularities as rotations of π are treated
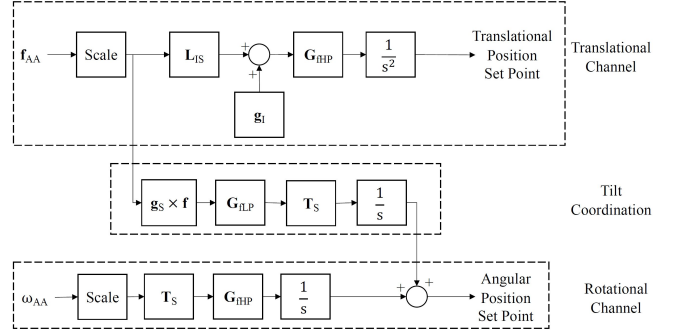
Figure 3. Classical washout for large angles.

as a special case, and distinct orientations represented by unit quaternions can be viewed as points on the surface of a unit 4D hypersphere, where distinct points represent distinct orientations (Ref. 22). Because of this representation, unit quaternions are used to replace Euler angles in classical washout to eliminate representational singularities encountered by every Euler angle convention over large ranges of angle. The small-angle approximations are removed to improve the accuracy of the washout algorithm when the simulator is at large angles. Figure 3 illustrates the block diagram for large-angle washout employing quaternions, which includes the translational, tilt coordination, and rotational channels. The following subsections discuss the changes made to each channel for large-angle washout.

Translational Channel (Large Angle)

For large-angle washout, the only modification that needs to be made to the translational channel is the conversion from the aircraft frame to the inertial frame. Figure 4 illustrates how small-angle washout used the rotation matrix. From Equation 1 $\boldsymbol{L_{IS}}$, which uses Euler angles, is replaced with a unit quaternion measure of rotation,

$$r(\boldsymbol{f}) = (-\boldsymbol{q}) \otimes \boldsymbol{f} \otimes (-\boldsymbol{q}^*) \qquad (15)$$

where $\boldsymbol{f}$ is the scaled specific force, $\boldsymbol{q}$ is the orientation of the simulator, and $\boldsymbol{q}^*$ is the associated conjugate quaternion, such that

$$\boldsymbol{q}^* = \begin{bmatrix} q_0 \\ -\boldsymbol{q_v} \end{bmatrix}. \qquad (16)$$

As a result of the modifications to the translational channel, the small-angle approximation version of tilt coordination from Equation 5 cannot be used, as the small-angle approximations are no longer valid.

Tilt Coordination (Large Angle)

Figure 5 illustrates modifications to the tilt coordination channel for small-angle washout and for large-angle washout. First, in the small angle washout, the gravity vector in the simulator frame, $\boldsymbol{g_S}$, was calculated by using the rotation matrix
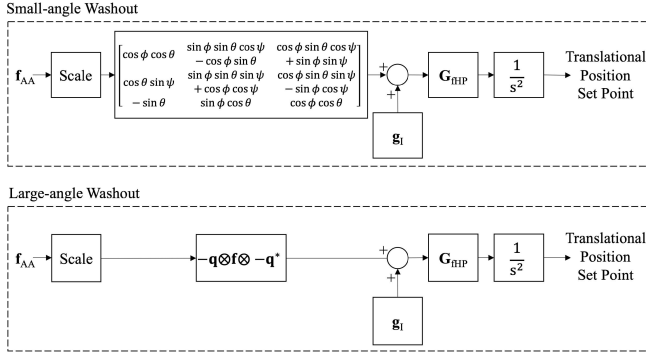
Figure 4. Translational channel (top) small-angle washout (bottom) large-angle washout.
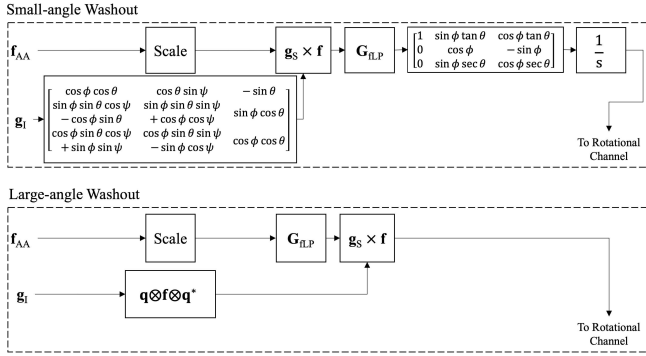

Figure 5. Tilt coordination (top) small-angle washout (bottom) large-angle washout.

L_{SI} from Equation 7, with the Euler angles of the simulator orientation. In the large-angle washout, the Euler angle rotation matrix is replaced by a quaternion rotation similar to Equation 15 from the translational channel.

The second change is that instead of converting the angular velocity output from the low-pass filter to rate of change of Euler angles and then integrating to produce Euler angles, the angular velocity is directly output from the tilt coordination channel. The third change is moving the low-pass filter to before the cross product, which is the location it is found in the small-angle simplification version of tilt coordination. Filtering the specific force instead of the angular velocity reduces unwanted oscillations in the tilt coordination velocity output. As before, the tilt coordination is a required input to the rotational channel of the algorithm.

Rotational Channel (Large Angle)

Figure 6 illustrates the small-angle washout rotational channel as well as the large-angle washout rotational channel. It is important to observe that the elimination of Euler angles results in the high-pass filtering occurring in angular velocity rather than rate of change of Euler angles. Filtering in angular velocity has been shown to have a small negative impact on the flight simulator's performance (Ref. 2). However, it also allows the addition of the outputs of the tilt coordination and
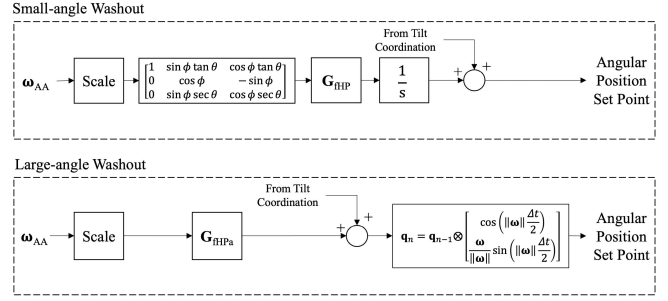
Figure 6. Rotational Channel (top) small-angle washout (bottom) large-angle washout.

rotational channel to occur in angular velocities, removing the error introduced by the addition of Euler angles.

Next, as the channel is using angular velocities instead of converting to rate of change of Euler angles, the matrix T_S is removed. After filtering, the angular velocity set point from tilt coordination is added to the rotational channel. To convert the angular velocity to an angular position set point expressed as a unit quaternion, a quaternion integrator is added, which is calculated using

$$q_n = q_{n-1} \otimes \begin{bmatrix} \cos(\|\omega\|\Delta/2) \\ \frac{\omega}{\|\omega\|}\sin(\|\omega\|\Delta/2) \end{bmatrix} \qquad (17)$$

where Δt is the timestep and q_{n-1} is the previous angular position set point, to produce an angular position set point.

Finally, the model of the pilot's vestibular system must be modified for large angles.

Vestibular Model (Large Angle)

To accommodate large angles, the vestibular system is modified by means of the calculation of the motion at the pilot's head. For the translational acceleration, the rotation matrix L_{SI} is replaced by a quaternion rotation. For the angles, the angular position is read as a quaternion, and the angular motion of the pilot's head ω_{SS} is calculated as

$$\omega_{SS} = 2q^* \otimes \dot{q} \qquad (18)$$

where $\dot{q}$, the quaternion rate, is given by

$$\dot{q} = \frac{q_n - q_{n-1}}{\Delta t} \qquad (19)$$

The transfer functions used to model the pilot's vestibular system do not require any modifications. Since the Atlas simulator (Refs. 5–7) is capable of unlimited rotation, which could be advantageous for rotorcraft training, an additional change to large-angle washout was made to create an "Unrestricted Angular Washout" algorithm.

Unrestricted Angular Washout

The high-pass filters on the rotational channel (Equation 6) restrict the rotational envelope of the simulator. Thus, to create an unrestricted angular washout algorithm the ω_n values of the rotational high-pass filter are set to zero thereby effectively eliminating the filter from the rotational channel. To prevent the algorithm from requesting velocities greater than hardware's capabilities, the saturation limit after scaling of the rotational channel remains at 32.2 deg/s.

METRICS

To evaluate the relative performance of small-angle washout, large-angle washout, and unrestricted angular washout, three metrics were used. The normalized Pearson correlation, NPC, proposed by Casas et al. (Ref. 13), is calculated by first calculating the Pearson correlation, PC:

$$\text{PC}(x,y) = \frac{\sum_{i=1}^{n}(x_i - \bar{x})(y_i - \hat{y})}{\sqrt{\sum_{i=1}^{n}(x_i - \bar{x})^2}\sqrt{\sum_{i=1}^{n}(y_i - \bar{y})^2}}, \quad (20)$$

where x and y represent the signals being correlated, $\hat{x}$ and $\hat{y}$ are the mean of x and y respectively, and n is the number of samples. The normalized Pearson correlation is then calculated as

$$\text{NPC}(x,y) = \frac{K}{1 + \text{PC}(x,y)} + 1 - \frac{K}{2}, \quad (21)$$

where $K = 1$. This results in a nonlinear metric which measures the correlation between the two signals. The nonlinearity penalizes negative cues, as these have a detrimental impact on the pilot's experience. The integral of the error between the aircraft and simulator pilot's vestibular responses and the maximum error between the vestibular responses are also calculated, as the normalized Pearson correlation fails for unvarying signals due to the uncorrelated noise in the signals. The third metric is the integral of the error ε defined as

$$\varepsilon(x,y) = \int |x - y| dt \quad (22)$$

These three metrics are used to compare the calculated vestibular response for the aircraft pilot and the simulator pilot undergoing a manoeuvre, and can give an indication of how closely the simulator pilots experience is to the experience of an actual aircraft pilot.

BENCHMARK CASES

To compare the performance of large-angle washout and small-angle washout, a series of manoeuvres was completed using two aircraft with different flight characteristics: the Cessna 172 and the Columbia 400. These aircraft provide examples of the performance of the algorithms for a small fixed-wing aircraft and an aerobatic aircraft. In the flight simulation program X-Plane 'piloted' by an experienced simulator engineer and pilot, each aircraft was controlled to perform the following manoeuvres: a coordinated turn, a cross-wind landing, a single-axis takeoff, a spiral dive, and a stall recovery. For the Columbia 400 an aerobatic manoeuvre with large angular velocities in roll and pitch was also performed.

As the primary concern for assessing the algorithm performance is avoiding negative cues to the pilot, it is preferable to have a scaled cue then an incorrect cue. The normalized Pearson correlation gives a measurement of the correlation of the simulator pilot's vestibular response with the aircraft pilot's vestibular response, but cannot be used in isolation, as there are cases, such as when the response is flat, for which the normalized Pearson correlation is not informative. Also, different washout algorithms may perform better for different degrees of freedom in the same manoeuvre, so judgement is necessary to determine which cues have more impact on the pilot for a given manoeuvre. For example, if there is low correlation in a degree of freedom but there is also little motion in that degree of freedom, improved correlation in a degree of freedom with larger cues can be of more importance. Table 3 summarizes a subjective comparison of the performance of the three washout algorithms. The algorithms are ranked in terms of relative performance for the Cessna 172 for the coordinated turn, cross-wind landing, single-axis takeoff, spiral dive, and stall recovery; and for the Columbia 400 for the aerobatic manoeuvre. Small-angle washout performs best for the manoeuvres with small angular velocity cues, and unrestricted angular velocity washout performs best for the manoeuvres with large angular velocity cues. Large angle washout performs worst for all the manoeuvres except the spiral dive, and the unrestricted angular velocity washout outperforms it for that manoeuvre.

For conciseness, the remainder of the paper will illustrate these conclusions while focussing on the single-axis takeoff (modest motion) and aerobatic (motion rich) manoeuvres.

Cessna 172 Single-axis Takeoff with Large-angle Washout

The single-axis takeoff manoeuvre, illustrated in Figure 7 consists of abrupt specific forces in the surge and sway degrees of freedom, that gradually return to zero, while the heave specific force oscillates. The angular velocities for all degrees of freedom fluctuate constantly throughout the manoeuvre, with roll having significant negative spikes in angular velocity. The performance metrics for the single-axis takeoff manoeuvre are listed in Table 4, and the vestibular response is provided in Figure 8.

For surge, the normalized Pearson correlation is similar for the small- and large-angle washout algorithms, with the integral of the error better for large-angle washout and the maximum error better with small-angle washout. Examining the vestibular response in Figure 8 shows that the two washout algorithms perform similarly in the beginning and end of the manoeuvre, but that large-angle washout matches the aircraft pilot's vestibular response more closely during the middle part.

Table 3. Ranked order of performance for each washout algorithm version for each manoeuvre.

Aircraft	Manoeuvre	Small-Angle Washout	Large-Angle Washout	Unrestricted Angular Velocity Washout
Cessna 172	Coordinated Turn	1	3	2
	Cross-wind Landing	1	3	2
	Single-axis Takeoff	2	3	1
	Spiral Dive	3	2	1
	Stall Recovery	1	3	2
Columbia 400	Acrobatics	2	3	1

It is likely that large-angle washout is an overall improvement in response, particularly as the metrics where it performed worse were still very similar to small-angle washout.

For sway, small-angle washout performs better for all metrics listed in Table 4, but the differences are small. Examining the vestibular response in Figure 8 shows that both algorithm versions perform similarly. There are differences in how the algorithm versions respond to some of the smaller peaks in specific force later in the manoeuvre, which may impact the pilot's perception. However as these are small the algorithm will require pilot testing to assess. For heave, as is expected, neither algorithm version follows the changes in specific force due to the limitations of the flight simulator.

For the angular velocity degrees of freedom, examining the vestibular response shows that for the majority of the manoeuvre there is minimal perceived motion. For the large spikes in the perceived angular velocity seen in the roll degree of freedom in Figure 8, both algorithm versions fail to fully reproduce them. Overall, with the significant motion in the manoeuvre occurring in surge and sway, the pilot's vestibular response for large-angle washout is closer to the aircraft pilot's vestibular response, and sway is similar for both algorithm types. Large-angle washout may provide improved performance overall for this manoeuvre; however, the majority of the metrics show that the response is similar or slightly worse than the small-angle washout response.

Columbia 400 Aerobatic Manoeuvre with Large-angle Washout

The Columbia 400 aerobatic aircraft was also used to perform the same set of manoeuvres. The performance metrics for these manoeuvres are also listed in Table 4. Small-angle washout outperforms large-angle washout for the majority of the metrics.

In addition to these manoeuvres, an aerobatic manoeuvre was performed that would not be possible with the Cessna 172. The aircraft motion at the pilot's head is illustrated in Figure 9 for all six degrees of freedom. The performance metrics are listed in Table 4 and the vestibular response is illustrated in Figure 10. For all the degrees of freedom with the most significant variations, the simulator is unable to produce motions that can closely replicate the aircraft pilot's vestibular
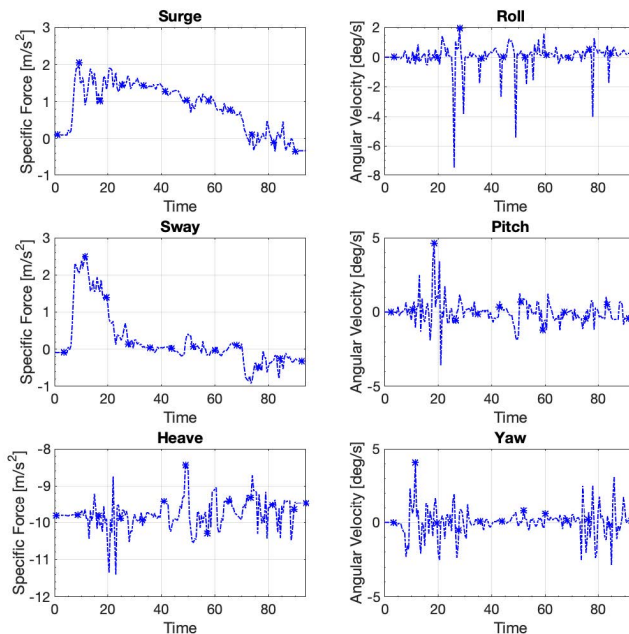

Figure 7. Aircraft motion at the pilot's head for a Cessna 172 completing a single-axis takeoff.

response, as the aerobatic manoeuvre is well outside the physical limitations of what the motion platform hardware could produce. For surge, small-angle washout performs better for all the metrics in Table 4, although examining the vestibular response in Figure 10 shows that neither algorithm could follow the response, so it is difficult to determine if there is a meaningful difference between the algorithm responses. For the heave response, small-angle washout performs better for the normalized Pearson correlation and the integral of the error, and large-angle washout performs better for the maximum error. Once again, however, both algorithms do not follow the aircraft pilot's response. For roll, large-angle washout performs better for the normalized Pearson correlation, the integral of the error, and the maximum error as listed in Table 4. Examining the vestibular response in Figure 10 shows that while the simulator is largely unable to follow the peaks of the angular velocity, large-angle washout captures the beginning of some peaks more accurately than small-angle washout, which may lead to some improvement.

Figure 11 illustrates the Euler angles for the aircraft orientation during the aerobatic manoeuvre. It is notable that there is
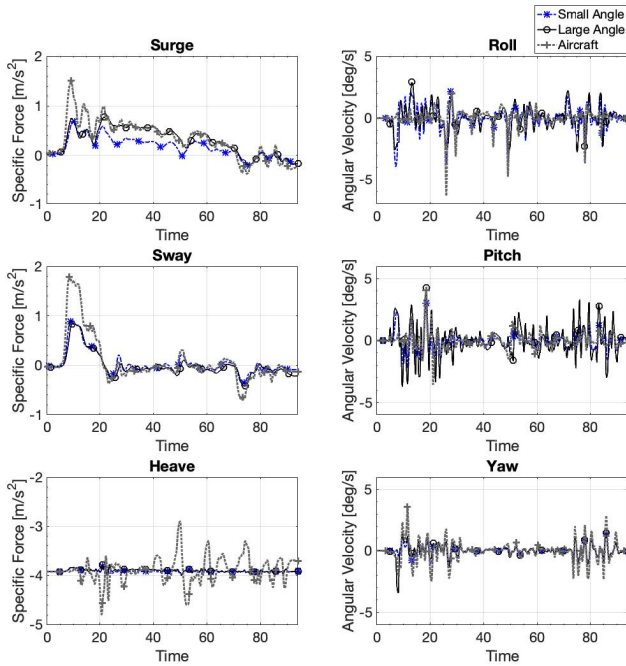
Figure 8. The vestibular response of the Cessna 172 aircraft pilot experiencing a single-axis takeoff, and the simulator pilot's vestibular response for small-angle washout and large-angle washout.

a discontinuity in the aircraft roll Euler angle from X-Plane 86 seconds into the manoeuvre, which is used to calculate the specific force acting on the pilot; however examining the vestibular response in Figure 10 illustrates that small-angle washout is not negatively impacted by the presence of this discontinuity, as there is no evidence of disruption in the response at that point in the vestibular response.

Overall, this manoeuvre is outside the bounds of the designed system, and neither algorithm version performs accurately. However, small-angle washout outperforms large-angle washout for the normalized Pearson correlation and the integral of the error.

Summary of Large-angle Washout Results

In all the cases shown, large-angle washout results in some improvement for some metrics, but overall does not present a compelling case for its use. The performance tradeoffs that were made for large-angle washout were intended to eliminate the problems that occur when the simulator was at sufficiently-large angles; however the design of classical washout prevents the simulator from approaching the singularity point, even with manoeuvres such as the Columbia 400's aerobatics. The simulator's angular position in ZYX-Euler angles for the aerobatics, illustrated in Figure 12, demonstrates that despite the large angular motion present in the aircraft orientation during the manoeuvre, the simulator motion is restricted so that the Euler angles are continuous at all times, so the potential singularities do not impact the performance of small-angle washout.

There are other improvements in large-angle washout, such as eliminating the addition of Euler angles and the small-angle
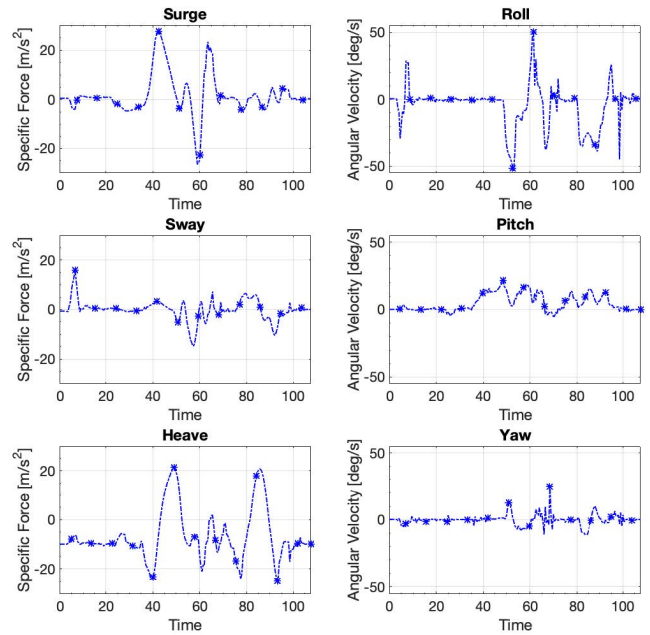

Figure 9. Aircraft motion at the pilot's head for the Columbia 400 aircraft pilot experiencing the aerobatic manoeuvre.

approximations, which should reduce the error source in the algorithm. However, the test cases show that these changes often do not result in an overall improvement after the performance tradeoffs caused by filtering at the angular velocity level.

Columbia 400 Aerobatic Manoeuvre with Unrestricted Angular Velocity Washout

The Columbia 400 aircraft completing the aerobatics manoeuvre shows the impact of removing the rotational channel high-pass filters in the implementation of unrestricted angular velocity washout. Figure 13 shows the angular position for each rotational degree of freedom as integrals of the angular velocity (not Euler angles) which illustrates that the simulator completes more than a full rotation in roll and nearly a full rotation in pitch, which is much more angular motion than what was present with the high-pass filter in place. The extended angular motion allows the corresponding vestibular responses for angular velocity to achieve peaks that were not previously possible, and allows the tilt coordination to act on different degrees of freedom for different parts of the manoeuvre, as the simulator orientation changes.

The metrics for the manoeuvre with unrestricted angular velocity, compared against small-angle washout and large-angle washout, are listed in Table 4. For all the rotational degrees of freedom, the unrestricted angular velocity washout improves the normalized Pearson correlation, the integral of the error, and the maximum error compared with small-angle washout. The results are mixed for the translational degrees of freedom, with surge and heave performing worse with unrestricted angular velocity washout for all metrics, while sway has an improved normalized Pearson correlation and maximum error,
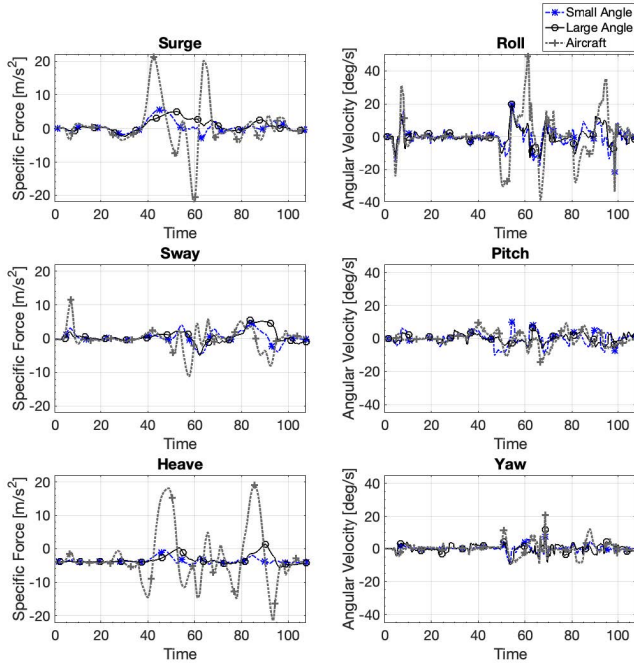
Figure 10. The vestibular response of the Columbia 400 aircraft pilot experiencing the aerobatic manoeuvre, and the simulator pilot's vestibular response for small-angle washout and large-angle washout.
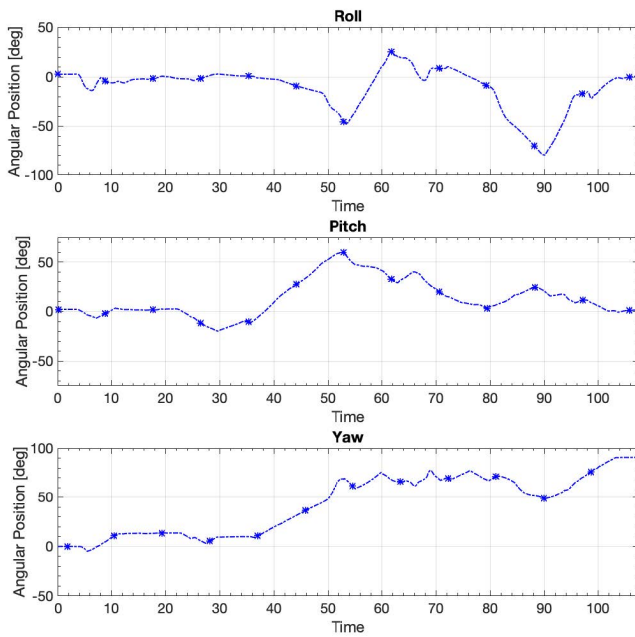

Figure 11. The aircraft's orientation in Euler angles for large-angle washout during the aerobatic manoeuvre in the Columbia 400.

with a worse result for the integral of the error. The vestibular response for the aircraft pilot subjected to small-angle washout and unrestricted angular velocity washout completing the aerobatic manoeuvre are illustrated in Figure 14. Particularly in roll, which has the most significant angular velocity cues, the unrestricted angular velocity washout matches the angular velocity peaks more accurately than small-angle washout and does not have the negative cues that are present in the small-angle washout vestibular response.

Heave, despite performing worse for all metrics, shows that for some of the peaks, unrestricted angular velocity washout is able to match some of the peaks much more accurately than small-angle washout. Capturing some of these peaks may be worth the overall reduction in the performance metrics. Surge performs worse for all metrics, and examining the vestibular response shows that particularly in the second half of the manoeuvre the unrestricted angular velocity washout pilot's vestibular response is not following the aircraft pilot's response. The performance reduction is likely due to the improved pitch performance, which may be dominating the response.

The relationship between the vestibular response for the simulator and the orientation of the gravity vector is illustrated in Figure 15. The first column of graphs shows the specific force vestibular response for the aircraft pilot and the simulator pilot for the unrestricted angular velocity washout and the second column of graphs shows the component of the simulator's gravity vector along each axis during the manoeuvre. The components of the gravity vector are significant to understanding the specific force vestibular response, as when the gravity vector is aligned with a translational degree of freedom ($\boldsymbol{a}_{AA} \approx \pm 9.81$ m/s^2), the effect of tilt coordination is
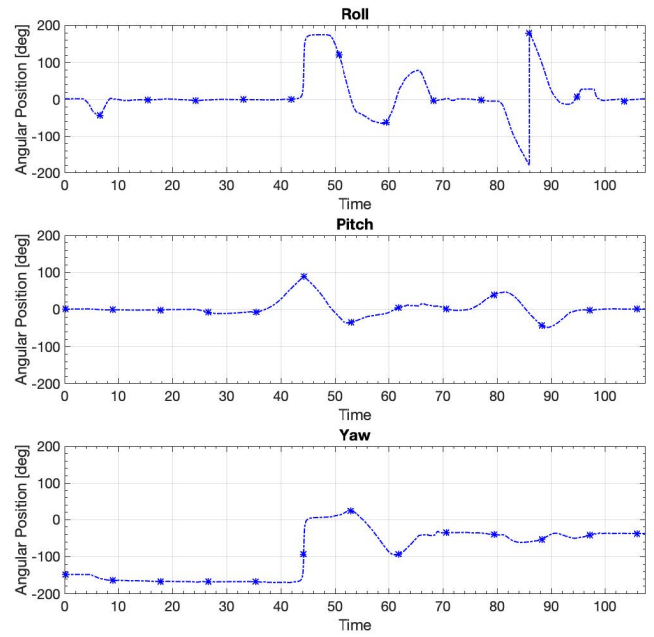
limited, as there is no way to increase the specific force applied to the pilot in those circumstances, as the maximum effect of gravity is already acting on that degree of freedom. Therefore, the simulator is limited to the translational acceleration, which is restricted due to the geometry of the simulator and the high-pass filters on the translational channel. In small-angle washout, the lack of tilt coordination is assumed to impact only the heave degree of freedom, as the small angular motion means that the gravity vector will be aligned with the heave axis, and only deviate from it by small angles. With the elimination of the effects of the high-pass filters, any translational degree of freedom can be aligned with the gravity vector during the course of the manoeuvre. It is important to remember that specific force is the force acting on the pilot from the simulator, and therefore the gravity component is in the opposite direction of the resulting specific force.

For surge, in Figure 14 at just over 40 seconds, the gravity component reaches its maximum, which corresponds with the large peak in the specific force. While the gravity component is at its limit, the simulator is unable to match the peak of the aircraft pilot's response, as it has reached its maximum specific force. For heave, the simulator does not follow the aircraft pilot's vestibular response for the first 40 seconds. During this time, the heave gravity component is maximized, as this axis is aligned with the gravity vector, which limits the range of specific force to what can be generated by the motion of the platform.

Overall, there is substantial improvement in the performance of the angular degrees of freedom. There is some reduction in performance in the translational degrees of freedom; however the response for both washout algorithms is not accurate as the manoeuvre being completed far exceeds the abilities of the simulator.
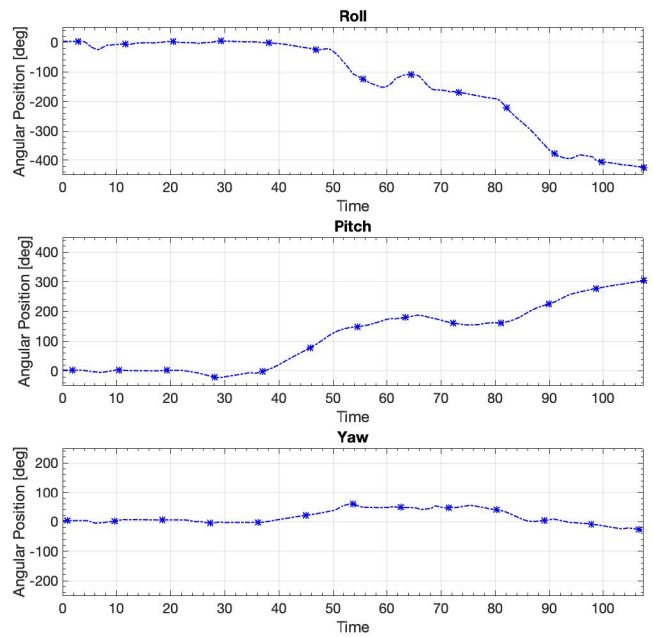
Figure 12. The flight simulator's orientation in Euler angles for large-angle washout during the aerobatic manoeuvre in the Columbia 400.

Cessna 172 Single-axis Takeoff with Unrestricted Angular Washout

The manoeuvres with the Cessna 172 were also run with the unrestricted angular velocity washout. The performance metrics for each manoeuvre are listed in Table 4. The single-axis takeoff manoeuvre is an example of a manoeuvre with limited angular velocity and significant specific force values. For the unrestricted angular velocity washout the normalized Pearson correlation is slightly worse for all degrees of freedom except heave. For the integral of the error, unrestricted angular velocity washout improves the performance for surge and yaw, but otherwise the performance is similar or worse. For the maximum error, the values are similar for most degrees of freedom, with small-angle washout performing better for sway and pitch. Examining the vestibular response provided in Figure 16 shows that the response for surge is similar for the two washout algorithms for the first 20 seconds, and then unrestricted angular velocity washout is much closer to the aircraft pilot's vestibular response, despite the reduction in performance metrics. For all other degrees of freedom, the response for the two types of washout appear to be extremely similar. Overall, the performance metrics indicate that for this small-angle manoeuvre, small-angle washout may be a better option, although the vestibular response indicates that this performance reduction may not be a major issue to the pilot's perception of the motion as the differences between the responses appear to be small.

Summary of Unrestricted Angular Washout

For manoeuvres with large angular velocities, there is a clear benefit to the unrestricted angular washout, as it improves the

Figure 13. The flight simulator's orientation calculated as the integral of the angular velocity for unrestricted angular velocity washout during the aerobatic manoeuvre in the Columbia 400.

performance for the rotational degrees of freedom, and usually without significant detriment to the translational degrees of freedom. For the manoeuvres with no significant angular velocity cues, the small-angle washout is likely the better option based on the performance metrics, although unrestricted angular washout does not seem to cause a large performance degradation. Further testing with pilots is necessary to confirm these results.

Summary of Benchmark Results

Table 4 contains the metrics for a single-axis takeoff manoeuvre and an aerobatic manoeuvre with large angular velocities, as examples of a manoeuvre with small angular motion cues and large angular motion cues respectively. For each metric the simulator pilot's vestibular response was compared against the aircraft pilots vestibular response for each degree of freedom. Then using the small-angle washout algorithm developed by Reid and Nahon (Ref. 2) as the baseline for the performance, the large-angle washout or unrestricted angular washout result was compared against it by subtracting the calculated metrics. When the difference column is positive, it indicates that large-angle washout or unrestricted angular washout performed better than small-angle washout for that degree of freedom. For the single-axis takeoff manoeuvre, large-angle washout and unrestricted angular washout both perform slightly worse than small-angle washout for almost all the degrees of freedom across all the metrics, indicating that small-angle washout performs best for this manoeuvre.

For the aerobatic manoeuvre, large-angle washout showed mixed results across the metrics as to whether it improved the response. However, unrestricted angular washout improved

Table 4. Performance metrics for the classical washout algorithms vs. small angle: correlation of small/large or small/unrestricted angular washout.

Washout	DOF	NPC	Diff.	Integral of Error [m/s^2] or [deg/s]	Difference [m/s^2] or [deg/s]	Maximum Error [m/s^2] or [deg/s]	Difference [m/s^2] or [deg/s]
Single-axis Takeoff Large-angle	Surge	1.01/1.02	-0.01	19.1/9.5	9.6	0.9/0.7	-0.2
	Sway	1.00/1.01	-0.01	12.9/14.2	-1.3	1.0/1.2	-.02
	Heave	1.97/1.89	0.08	17.7/17.7	0.0	1.1/1.0	0.1
	Roll	1.15/1.25	-0.10	51.8/63.4	-11.6	4.0/3.8	0.2
	Pitch	1.13/1.21	-0.08	39.0/72.7	-33.7	2.6/3.7	-1.1
	Yaw	1.01/1.06	-0.05	26.7/28.4	-1.7	2.5/2.4	0.1
Single-axis Takeoff Unrestricted Angular	Surge	1.01/1.02	-0.01	19.1/9.5	9.6	0.9/0.8	-0.1
	Sway	1.00/1.01	-0.01	12.9/14.2	-1.3	1.0/1.3	-.03
	Heave	1.97/1.89	0.08	17.7/17.7	0.0	1.1/1.0	0.1
	Roll	1.15/1.25	-0.10	51.8/63.6	-11.8	4.0/3.8	0.2
	Pitch	1.13/1.21	-0.08	39.0/72.9	-33.9	2.6/4.0	-1.4
	Yaw	1.01/1.05	-0.04	26.7/25.5	1.2	2.5/2.4	0.1
Aerobatics Large-angle	Surge	1.23/1.40	-0.17	366.7/403.0	-36.3	22.6/24.7	-2.1
	Sway	1.30/1.74	-0.17	213.7/270.8	-57.1	11.2/12.6	-1.4
	Heave	1.10/1.25	-0.15	550.7/566.4	-16.4	21.4/20.4	1.0
	Roll	1.18/1.11	0.07	735.8/698.1	37.7	44.3/42.3	2.0
	Pitch	1.35/1.76	-0.41	406.6/324.4	82.2	14.0/12.2	1.8
	Yaw	1.19/1.23	-0.04	213.7/283.0	-69.3	14.2/10.7	3.5
Aerobatics Unrestricted Angular	Surge	1.23/1.29	-0.06	366.7/420.5	-53.8	22.6/25.8	-3.2
	Sway	1.30/1.24	0.06	213.7/275.4	-61.7	11.2/9.5	1.7
	Heave	1.10/1.21	-0.11	550.7/569.9	-19.2	21.4/24.5	-3.1
	Roll	1.18/1.01	0.17	735.8/475.5	260.3	44.3/25.1	19.2
	Pitch	1.35/1.05	0.30	406.6/211.9	194.7	14.0/7.1	6.1
	Yaw	1.19/1.09	0.10	213.7/212.4	1.3	14.2/9.0	5.2

results for the angular degrees of freedom for all the metrics, with mixed results for the translational degrees of freedom. Figure 14 illustrates the vestibular response for the aircraft pilot, the simulator pilot using small-angle washout, and the simulator pilot using unrestricted angular washout. While the simulator is unable to match the peaks of the specific force cues in the translational degrees of freedom due to hardware limitations, particularly in the heave and roll degrees of freedom, unrestricted angular washout matches the peaks of the motion cues much more closely than small-angle washout, and has a similar response for the other degrees of freedom. Therefore, unrestricted angular washout should result in a better experience for the simulator pilot compared to small-angle washout for this manoeuvre with large angular motion cues.

For aircraft manoeuvres with large angular motion, unrestricted angular washout has the best performance of the three washout algorithms examined. While large-angle washout does have some performance benefits compared with small-angle washout for some manoeuvres with large angular motion, unrestricted angular washout outperforms large-angle washout for these manoeuvres, and for simulators with unrestricted angular motion envelopes, unrestricted angular washout should be used when simulating these large angular

motion manoeuvres. For aircraft manoeuvres with small angular motion, small-angle washout has the best performance of the three washout algorithms. However, unrestricted angular washout's performance is comparable to small-angle washout, and therefore it is also a reasonable choice for small-angle manoeuvres. Large-angle washout does not perform well for small angular manoeuvres compared to the other two washout algorithms, and should not be used for these manoeuvres.

DISCUSSION AND CONCLUSION

The objectives of this work were:

1. To remove the small-angle restrictions and extend the range of angular motion for classical washout.

2. To demonstrate the performance of large-angle classical washout in simulation.

Objective 1: Extension of Classical Washout

Initial extensions to classical washout that resulted in large-angle washout were described, and simulation results were
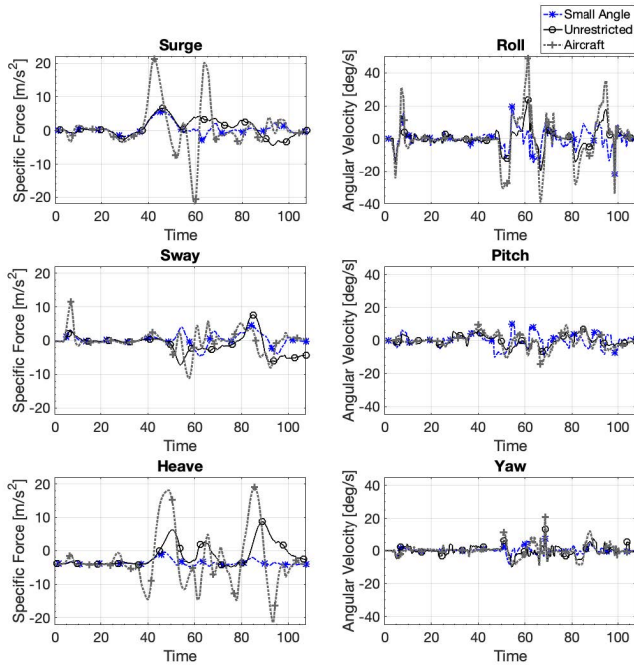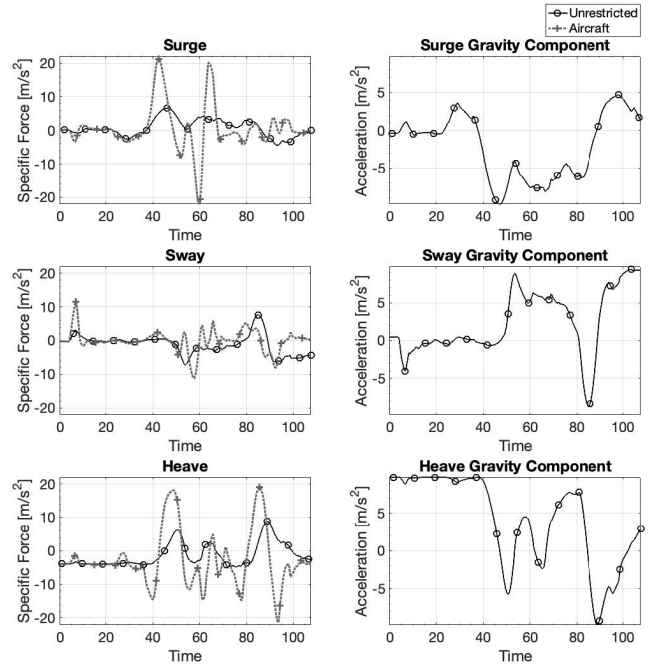
Figure 14. The vestibular response of the Columbia 400 aircraft pilot experiencing the aerobatic manoeuvre, and the simulator pilot's vestibular response for small-angle washout and unrestricted angular velocity washout.

used to compare the performance for small-angle manoeuvres. Subsequently, to improve performance, classical washout was extended to unbounded rotation by the removal of the high-pass filters for the rotational channel. The contribution related to this objective was extending classical washout to allow a larger angular range of motion. This washout model used quaternions instead of Euler angles and eliminated the small-angle approximations present in small-angle washout. Large-angle washout overall did not perform as well as small-angle washout for the manoeuvres considered; however, unbounded angular velocity washout improved performance compared to small-angle washout for manoeuvres with large angular motion, and achieves similar performance at small angles.

Objective 2: Performance Validation

Large-angle classical washout and unrestricted angular classical washout were simulated and compared against the performance of small-angle classical washout. The main contribution related to this objective was simulated validation of the performance of classical washout with an extended angular range of motion. Large-angle classical washout did not perform well compared to small-angle washout, and therefore was not a feasible replacement for that algorithm. The unrestricted angular washout performed well compared to small angle washout, particularly with manoeuvres that contain large angular velocity cues. Unrestricted angular washout shows clear advantages for use with manoeuvres that have large angular motion, and is comparable to small-angle washout in performance for small-angle cues.

Figure 15. The vestibular response of the Columbia 400 aircraft pilot experiencing the aerobatic manoeuvre, and the simulator pilot's vestibular response for washout with unrestricted angular velocity, and the components of gravity acting on the simulator.

Future Work

The following are suggested as potential areas of future work:

1. Hardware testing of unrestricted angular washout with pilot evaluation. All the tests conducted in this thesis were performed with numerical metrics and subjective evaluation based on the graphed vestibular response. Pilot-in-the-loop testing would provide additional evaluation of the washout modifications.

2. Tuning the transfer function coefficients for improved washout performance. Several tuning mechanisms for washout, including genetic algorithms, fuzzy logic, and particle swarm optimization that have been applied successfully to small-angle classical washout. The described implementation of unrestricted angular washout uses the transfer function coefficients that were reported by Reid and Nahon, and further improvements could be accomplished with additional tuning.

3. Development of an adaptive washout algorithm for large-angle washout. Adaptive washout is less commonly used than classical washout due to its complexity. However, it has good performance that could be improved with extending it to large angles.

ACKNOWLEDGMENTS
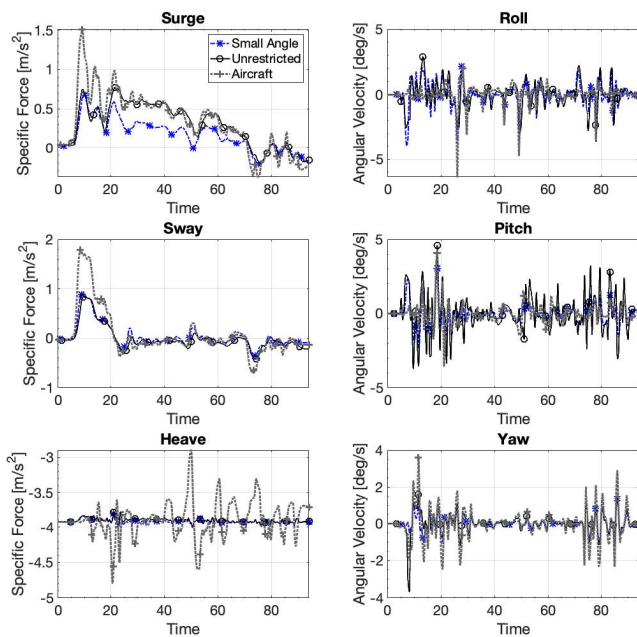
Figure 16. The vestibular response of the Cessna 172 aircraft pilot experiencing a single-axis takeoff, and the simulator pilot's vestibular response for small-angle washout and unrestricted angular velocity washout.

REFERENCES

1. Reid, L. D., and Nahon, M. A., "Flight Simulation Motion-Base Drive Algorithms: Part 1 - Developing and Testing the Equations," Technical report, UTIAS, 1985.

2. Reid, L. D., and Nahon, M. A., "Flight Simulation Motion-Base Drive Algorithms: Part 2 - Selecting the System Parameters," Technical report, UTIAS, 1986.

3. Reid, L. D., and Nahon, M. A., "Flight Simulation Motion-Base Drive Algorithms: Part 3 - Pilot Evaluations," Technical report, UTIAS, 1986.

4. Schlimm, K. A., "A model for situational awareness in aircraft upset prevention and recovery," 15th AIAA Aviation Technology, Integration, and Operations Conference, 2015.

5. Irani, R. A., Schut, N., Hayes, M. J. D., and Langlois, R. G., "A Novel Flight Simulator Capable of Unbounded Rotation," *Proceedings of the 2017 IEEE International Symposium on Systems Engineering (ISSE), Vienna, Austria*, October 11-13, 2017.

6. Copeland, Z., Jung, B., Hayes, M. J. D., and Langlois, R. G., "Full-scale Atlas Motion Platform: Structure, Actuation, and Control," *International Journal of Mechanisms and Robotic Systems*, Vol. 3, (2/3), 2016, pp. 94–112.

7. Hayes, M. J. D., and Langlois, R. G., "Atlas: A Novel Kinematic Architecture for Six DOF Motion Platforms," *Trans. Can. Soc. Mech. Eng.: Selected Papers of the 3*rd

8. Micomonico, M., Hayes, M. J. D., Irani, R. A., and Langlois, R. G., "Classical Washout Using Quaternions," CCToMM Mechanisms, Machines, and Mechatronics M³ Symposium, Montréal, QC., Canada, May 16-17 2019.

9. Asadi, H., Mohammadi, A., Mohamed, S., Lim, C. P., Khatami, A., Khosravi, A., and Nahavandi, S., "A Particle Swarm Optimization-based washout filter for improving simulator motion fidelity," 2016 IEEE International Conference on Systems, Man, and Cybernetics (SMC), 2016.

10. Asadi, H., Mohamed, S., Zadeh, D. R., and Nahavandi, S., "Optimisation of nonlinear motion cueing algorithm based on genetic algorithm," *Vehicle System Dynamics*, Vol. 53, (4), 2015, pp. 526–545.

11. Asadi, H., Mohamed, S., and Nahavandi, S., "Incorporating human perception with the motion washout filter using fuzzy logic control," *IEEE/ASME Transactions on Mechatronics*, Vol. 20, (6), 2015, pp. 3276–3284.

12. Grant, P. R., and Reid, L. D., "PROTEST: An expert system for tuning simulator washout filters," *Journal of Aircraft*, Vol. 34, (2), 1997, pp. 152–159.

13. Casas, S., Coma, I., Riera, J. V., and Fernndez, M., "Motion-Cuing Algorithms: Characterization of Users Perception," *Human Factors,* vol 57, pp 144-162, 2015.

14. Keshavarz, B., Ramkhalawansingh, R., Haycock, B., Shahab, S., and Campos, J., "Comparing simulator sickness in younger and older adults during simulated driving under different multisensory conditions," *Transportation research part F: traffic psychology and behaviour*, Vol. 54, 2018, pp. 47–62.

15. Cleij, D., Venrooij, J., Pretto, P., Pool, D. M., Mulder, M., and Bülthoff, H. H., "Continuous subjective rating of perceived motion incongruence during driving simulation," *IEEE Transactions on Human-Machine Systems*, Vol. 48, (1), 2017, pp. 17–29.

16. Dalmeijer, W., Miletovic, I., Stroosma, O., and Pavel, M., "Extending the Objective Motion Cueing Test to Measure Rotorcraft Simulator Motion Characteristics," *Surge*, Vol. 7, 2017, pp. 6.

17. Young, L. R., and Meiry, J. L., "A revised dynamic otolith model," *Aerospace medicine*, Vol. 39, (6), 1968, pp. 606–608.

18. Zacharias, G. L., "Motion cue models for pilot-vehicle analysis," Technical report, Bolt Beranek and Newman Inc Cambridge MA Control Systems Dept., 1978.

CCToMM Symposium on Machines, Mechanisms, and Mechatronics, Vol. 29, (4), 2005, pp. 701–709.

19. Asadi, H., Mohamed, S., Lim, C. P., and Nahavandi, S., "A review on otolith models in human perception," *Behavioural brain research*, Vol. 309, 2016, pp. 67–76.

20. Young, L., "Model for vestibular adaptation to horizontal rotation," *Aerospace Medicine*, Vol. 40, 1969, pp. 1076–1080.

21. Asadi, H., Peng, S. M. C., Lim, Nahavandi, S., and Nalivaiko, E., "Semicircular canal modeling in human perception," *Reviews in the Neurosciences*, Vol. 28, (5), 2017, pp. 537–549.

22. Craig, J., *Introduction to Robotics, Mechanics and Control*, Pearson Prentice Hall, Upper Saddle River, NJ, USA, 2005.